

## Article

# Design of an Automatic Sealing Mechanism for Extraterrestrial Sample-Collecting Robot

Yujian Mu <sup>1,2</sup>, Zihao Yuan <sup>1</sup>, Ruinan Mu <sup>1</sup>, Haifeng Zhao <sup>1,3,\*</sup> , Zhitao Ning <sup>1</sup>, Xihan Li <sup>1</sup>, Tianyue Gan <sup>1,3</sup>, Tao Du <sup>1,3</sup>, Zhiqiang Wang <sup>1</sup>, Rujin Han <sup>1</sup> and Zhenxing Shen <sup>2,\*</sup> 

<sup>1</sup> Key Laboratory of Space Utilization, Technology and Engineering Center for Space Utilization, Chinese Academy of Sciences, Beijing 100045, China; res9138@dingtalk.com (Y.M.); yuanzihao@csu.ac.cn (Z.Y.); muruinan@csu.ac.cn (R.M.); ningzhitao@csu.ac.cn (Z.N.); lixihan@csu.ac.cn (X.L.); gantianyue23@mailsucas.ac.cn (T.G.); dutao22@csu.ac.cn (T.D.); wangzhiqiang@csu.ac.cn (Z.W.); hanrujin@csu.ac.cn (R.H.)

<sup>2</sup> Yanshan University, Qinhuangdao 066104, China

<sup>3</sup> University of Chinese Academy of Sciences, Beijing 101408, China

\* Correspondence: hfzhao@csu.ac.cn (H.Z.); shenzx@ysu.edu.cn (Z.S.)

**Abstract:** Returning extraterrestrial samples to Earth for analysis is crucial for planetary geological research and resource utilization. However, during their return journey, these samples undergo significant environmental changes, such as varying pressure, temperature, impact, and vibration. Hence, a dependable sealing technique that preserves sample integrity without requiring high-powered tools is necessary. This article aims to develop an automatic sealing system for collecting extraterrestrial samples, conducting parametric design and mechanical analysis on two types of proposed sealing structures with minimal sealing force as the benchmark. Additionally, the system will undergo validation through sealing and leakage detection experiments. An automated sealing system, capable of storing samples in multiple sampling tubes, is assembled for the extraterrestrial sampling device.

**Keywords:** extraterrestrial sample; planetary sample storage; sealing design; coring mechanism; automatic sealing mechanism; terrestrial robot



**Citation:** Mu, Y.; Yuan, Z.; Mu, R.; Zhao, H.; Ning, Z.; Li, X.; Gan, T.; Du, T.; Wang, Z.; Han, R.; et al. Design of an Automatic Sealing Mechanism for Extraterrestrial Sample-Collecting Robot. *Aerospace* **2024**, *11*, 517. <https://doi.org/10.3390/aerospace11070517>

Academic Editor: George Z. H. Zhu

Received: 13 May 2024

Revised: 19 June 2024

Accepted: 22 June 2024

Published: 26 June 2024



**Copyright:** © 2024 by the authors. Licensee MDPI, Basel, Switzerland. This article is an open access article distributed under the terms and conditions of the Creative Commons Attribution (CC BY) license (<https://creativecommons.org/licenses/by/4.0/>).

## 1. Introduction

Extraterrestrial samples hold vital insights into planetary evolution and may contain volatile substances like water, ice, and organic matter. Thus, ensuring their return is highly localized and uncontaminated has become the critical determinant of success or failure in extraterrestrial sampling missions.

Various sealing configurations are available for extraterrestrial sample containers, including O-type rubber seals, knife-edge seals, brazed seals, explosion-welded seals, and shape-memory alloy seals. Rubber-ring seal structures are formed by extruding rubber to create the seal. For example, the Soviet Union's lunar probes Luna 16 [1–3], Luna 20 [4], and Luna 24 [5], as well as Japan's asteroid probe Hayabusa I [6,7], employed a single O-type rubber seal and double Viton O-ring seals. The sampling and sealing methods employed by Luna-16, Luna-20, and Luna-24 are essentially identical. The sealing container is a cylindrical structure located inside the return capsule, with its opening direction aligned with the direction of the capsule door. The rubber ring is installed on the cover of the sealing container. During sealing, the return capsule cover is closed, and the rubber ring is compressed by the barrel of the sample sealing container to achieve sealing. The double Viton O-rings of Hayabusa I are also positioned on the inner lib, with sealing achieved through compression.

The knife-edge seal is formed by inserting a knife-edge blade into the soft metal, thereby creating a vacuum seal through the deformation of the soft metal. This sealing

structure, widely employed in sample containers during the Apollo mission [8,9], involves inserting a stainless-steel blade into an indium–silver alloy to form the seal. Similarly, the sealing technique employed in Hayabusa II [10,11] achieves sealing by pressing the inner edge of an aluminum alloy container against the curved lid made of pure aluminum. The automatic sealing device in the Change 5 [12–14] probe adopts knife-edge sealing as the primary sealing method and O-ring sealing as the secondary method, an approach known as redundant sealing. The Apollo Lunar Sample Return Container (ALSRC) [9] employed in the Apollo missions also utilized a redundant sealing structure comprising two rubber-ring seals and a knife-edge seal.

Brazing sealing is kind of sealing approaches created by melting brazing material between multiple metal surfaces using a heating device, establishing a bond between them. Following the seal failure induced by lunar dust in the Apollo mission's lunar sample return container, NASA suggested a molten metal seal as a solution. In this method, indium alloy is heated until molten, enabling it to blend with lunar dust and form a monolithic structure with the knife-edge design once the alloy cools down. Additionally, NASA proposed a special double-wall brazed seal container for Mars sample collection [15,16], consisting of upper and lower lid bodies containing brazing material and an inner and outer cylinder. The internal lid and barrel are brazed together using induction coil heating. Younse [17,18], Bao [19], Backes [20], and Wang [21] have also independently proposed similar brazed seal structures. Explosively welded joints are achieved by explosively accelerating one plate to impact a second plate, and NASA designed a double-walled can with a geometry very similar to the one proposed for the Mars Sample Return Mission [22,23]. Zhang et al. [24] proposed an improvement program for cylindrical vessels with explosion-welded seals. The proposed sealing mechanism can be utilized to perform autonomous sampling missions in extraterrestrial environments. Currently, Honeybee have developed sample manipulation systems and sealing mechanisms for Mars sample return missions, which provide reference recommendations for the Mars 2020 program [25].

The principle of the shape-memory alloy (SMA) sealing solution revolves around manipulating the deformation of the alloy through temperature changes to achieve sealing within a specific structure. A commercial Nitinol shape-memory alloy plug, designed by InstaPlug, activates preformed fins when heated. These fins press into the inner wall of the tube, forming a hermetic seal [26,27]. Wang et al. [28] proposed an SMA-based sealing system. When subjected to controlled heating, the SMA component contracts in diameter. The inner wall of the SMA O-ring exerts pressure on the container's wall, resulting in a decrease in the canister's diameter. Consequently, the canister wall compresses against the knife edge, enabling the insertion of the knife edge into the inner wall of the container to create a vacuum seal. For the Mars 2020 mission, NASA utilized the convex seal structure proposed by Redmond et al. [29,30]. The complete structure includes a seal cup, ferrule, ferrule retainer, ferrule retaining ring, spacer, seal cup retaining ring, and tube-retention spring finger. During sealing, the ferrule is pushed down the seal cup, traveling along the interior ramp, which expands the seal. On the outer side of the seal cup, there is a sharp circumferential "tooth" that presses into the interior of the sample tube as the seal cup expands, thus forming the seal. As part of the Mars 2020 mission, the Perseverance Rover utilizes the sampling and caching subsystem (SCS) to facilitate the collection, processing, storage, and eventual drop-off of multiple samples [31]. Yang et al. [32] also designed a lunar surface sampling system capable of sampling a large area on the lunar surface, which can realize the functions of drilling, sampling, replacing and recycling sampling tubes.

In this work, an autonomous sealing system is proposed as a vital component for the robotic mobile sampling device. This sealing system enables individual sealing for multi-objects operating from different geological sampling areas. It consists of a rotating mechanism of sample tubes, rotating mechanism of sealed end caps, and external bracket. The feasibility of the proposed system is confirmed through the design and manufacturing of a prototype, which undergoes verification in the laboratory. The influence of seal geometric configuration on seal actuation force is systematically investigated via the finite element

analysis (FEA) method, and the validity of the results is confirmed by in-laboratory experiments. The long-term leakage rate of the seal configuration is measured experimentally, and the long-term stability of the seal structure is verified.

## 2. Robotic System Design

### 2.1. System Description

The robotic system can automate the sampling and sealing of extraterrestrial samples. Depending on the specific mission requirements, the number and size of sample tubes carried within the sealing mechanism can be adjusted to accommodate samples collected from different locations and with varying volumes. It consists of a sealing mechanism, a coring mechanism, and a mobile platform, as shown in Figure 1. The terrestrial robots convey the entire system to the designated task location. The coring mechanism drills at specific spots using the coring bit, while the sealing mechanism completes the sealing of the drill samples.

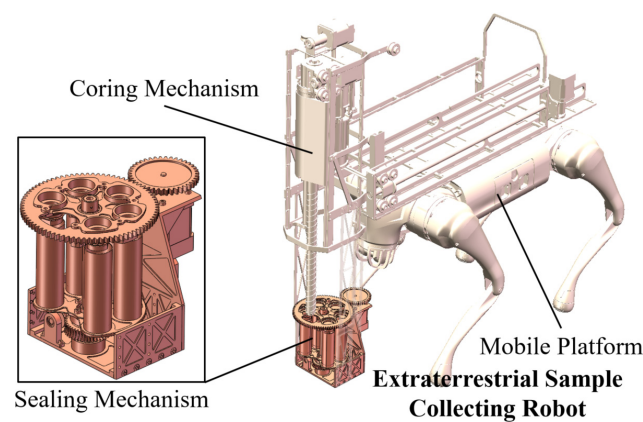


**Figure 1.** Sealing system for extraterrestrial sampling.

The automatic sealing mechanism on robotic system consists of the rotating mechanism of sample tubes, rotating mechanism of end caps, and an external bracket. The rotating mechanism of the sample tubes serves to store both sample-filled and empty tubes during non-operational periods.

### 2.2. System Workflow

During operation, this mechanism rotates the sample tube into position to receive the sample drilled by the coring mechanism. The rotating mechanism of the sample end cap is employed to rotate the sealing end cap directly above the sample tube in preparation for subsequent sealing. External brackets are utilized to maintain the stability of the entire system.

The overall assembly of the sealing system is depicted in Figure 2. Complete system weight is 326 g.

This system is based on the drilling and sampling method and is tightly integrated with the drilling system. The workflow is depicted in Figure 3, divided into four main steps: receiving the extraterrestrial sample, aligning the sealing end cap, executing the sealing, and resetting. During the sealing process, the sample tube is first rotated to the lower part of the drill pipe to receive the sample from the sampling drill pipe. Simultaneously, the seal end-cap storage area is rotated to a specific position so that the seal end cap is aligned directly above the seal canister. At this point, the sampling drill pipe, seal end cap, and seal canister are all axially aligned. The drill rod is lowered, pushing the sealing end cap into the sealing canister within the sealing end-cap storage area. As the process continues, sealing is achieved by an interference fit between the cutter and the seal cartridge. Subsequently, the drill tube rises, and both the seal end-cap storage area and sample tube storage area are reset, ready for the next sampling cycle. The next sampling cycle will take

the opposite direction of rotation from the previous cycle, which will cancel out some of the rotation error.

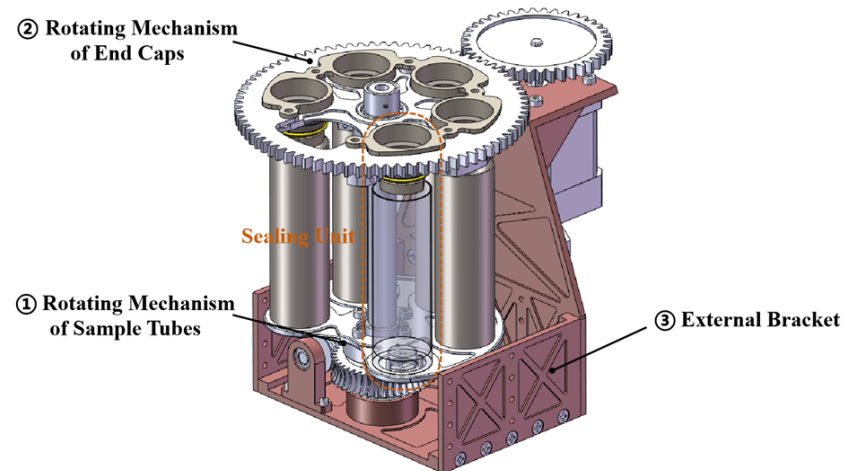


Figure 2. Sealing mechanism.

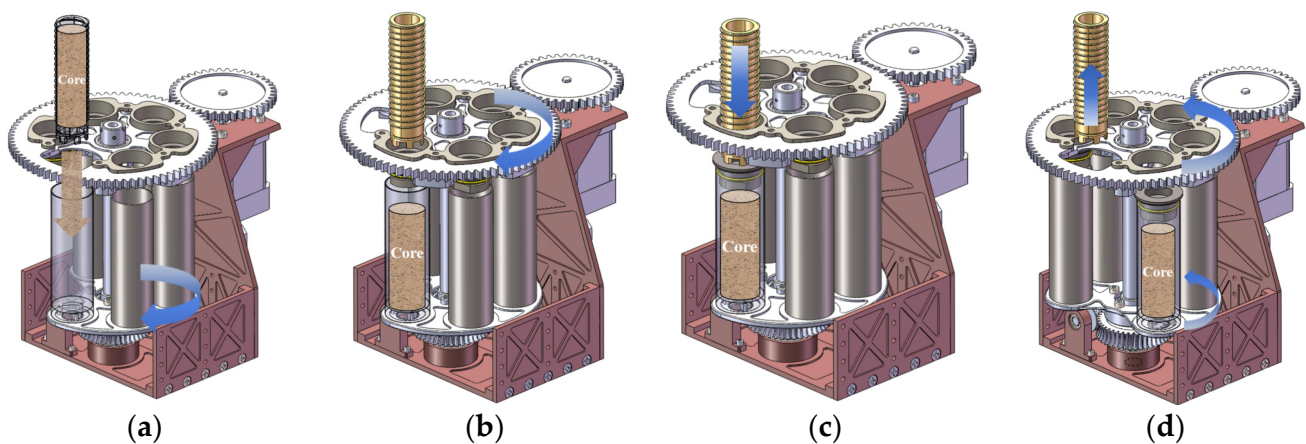
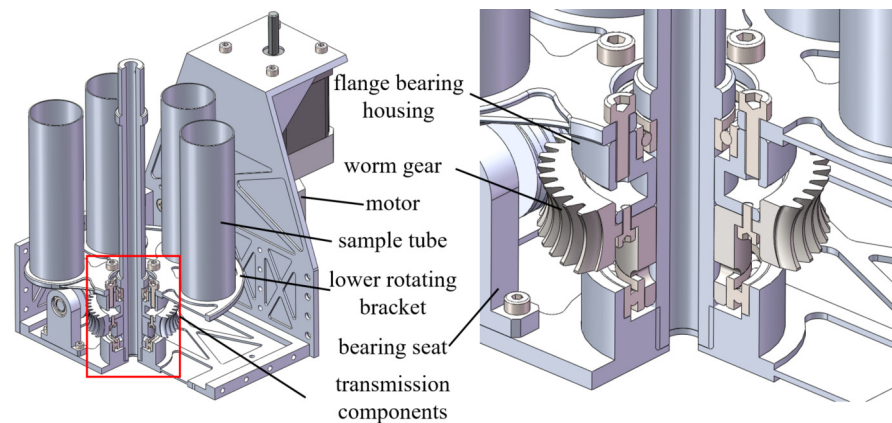


Figure 3. Schemes of automatic sealing system workflow: (a) receiving the extraterrestrial sample, (b) aligning the sealing end cap, (c) executing the sealing, and (d) reset, waiting for the next sample sealing task.

### 2.3. Sealing Mechanism Design

#### 2.3.1. Rotating Mechanism of Sample Tubes

The rotating mechanism of sample tubes is one of the operating components of the proposed autonomous sealing system. This component has two main functions: storing the sample tubes and driving their rotation. To realize the specific operations, the mechanical structure of this component is mainly assembled by: (1) the sample tube bracket and (2) rotary drive system. As shown in Figure 4, the tubes are securely fixed onto the lower rotating bracket in a circular arrangement using screws. The lower rotating bracket is connected to the worm gear via screws through flange bearing housing. Deep groove ball bearings are assembled on the upper end face of the flange bearing housing and the lower end face of the worm gear to ensure synchronization and concentricity during rotation. Additionally, worm gear, bearing, coupling, and other transmission components are assembled on the side of the worm gear through the bearing housing to achieve the precise positioning and rotation of the sample tubes. The number and size of sample tubes can be adjusted according to task requirements.



**Figure 4.** Rotating mechanism of sample tubes.

### 2.3.2. Rotating Mechanism of End Caps

The rotating mechanism of end caps is another operational component of the autonomous sealing system. Similar to the rotating mechanism of sample tubes, the rotating mechanism of end caps is utilized for storing the end caps and driving their rotation. Its overall structure is depicted in Figure 5. The sealing end caps are mounted on the upper rotating bracket in a circumferential distribution, corresponding one-to-one with the sample tubes directly underneath. This arrangement can be adjusted based on factors such as the number and size of sample tubes. In this design, the upper rotating bracket is spaced at intervals of  $60^\circ$  to accommodate the circumferential distribution of five sealing end caps, with shaped drilling holes reserved for interaction with the drilling mechanism. Three torsion spring-driven jaws, spaced  $120^\circ$  apart, secure each sealing end cap, with the upper section anchored by a hollow pressure plate. This installation ensures the stability of the sealing end caps in the non-operational state and prevents interference between components during the sealing process. The upper rotating bracket features a large gear fixed on its outer ring, which is driven by a pinion transmission assembly to enable the precise rotational positioning of the end caps. Bearings are installed at both ends of the upper rotating bracket, nested in the upper end of the center shaft, ensuring synchronization and concentricity of the rotation of the aforementioned components to prevent an eccentric rotation that may affect the seal. A retaining ring is mounted on the top end of the center shaft to ensure the stability of the overall rotating mechanism. The jaws are positioned in corresponding locations on the upper rotation bracket through studs, with the upper end face of the jaws in contact with the lower end face of the upper rotation bracket. Torsion springs are installed in corresponding positions of the upper rotation bracket, just below the jaws, ensuring that the jaws are installed in the same plane.

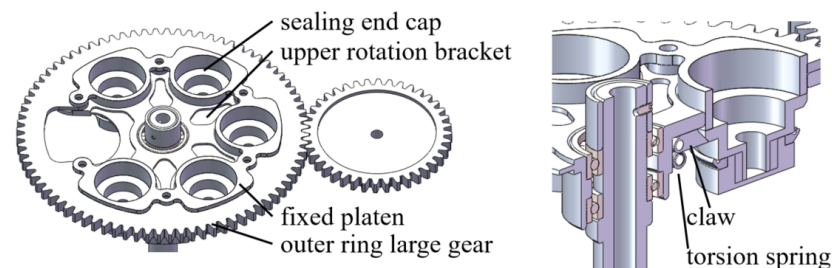


**Figure 5.** Rotating mechanism of end caps.

### 2.3.3. External Bracket

The whole system needs to be matched with the coring mechanism above; so it adopts a half package design to allow space above, the bracket side plate (left and right), back plate, and bottom plate are connected together using screws, and the center shaft is threaded onto

the bottom plate. The bracket's backplate is designed with rib plates to counterbalance the influence of the mounted drive motor on overall stability. Weight reduction design is conducted while maintaining operational stability.

### 3. Seal Design

In this section, two types of seal combination structures with different deformation mechanisms are designed, including a lateral non-sliding seal and lateral sliding seal as the classification of the mechanism.

#### 3.1. Lateral Non-Sliding Seal

The lateral non-sliding seal structure comprises two main components: the seal cup and the ferrule, as depicted in Figure 6. This sealing mechanism establishes a seal between the outer knife edge of the seal cup and the inner wall of the sample tube through metal extrusion, resulting in plastic deformation. The specific structural details are delineated in Figure 7. During the sealing process, a vertical downward force is applied to the upper face of the ferrule. The ferrule spacer and circlip ensure that the ferrule moves only downward. Inside the sealing cup, there exists a ramp profile opposite the outer knife edge, sized and shaped to allow radial outward contact with the seal cup wall. The ferrule is maintained in the sealing position, providing continuous sealing retention force.

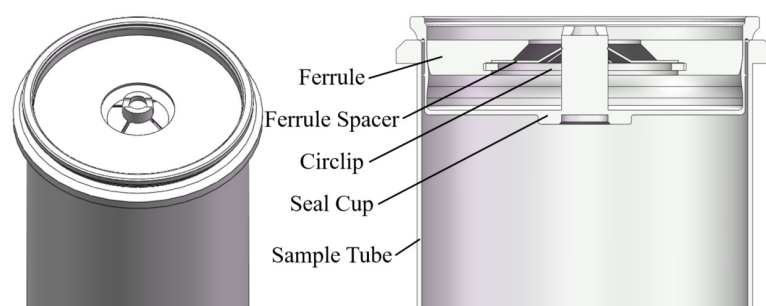


**Figure 6.** Lateral non-sliding seal.

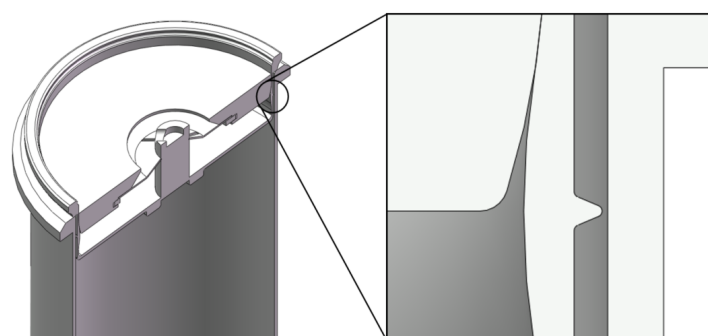


**Figure 7.** Detailed structure.

#### 3.2. Lateral Sliding Seal

The lateral sliding seal structure comprises a sealing end cap and a sample tube. The sealing cap includes a locking end cap, a sealing ring, and a locking base, as illustrated in Figure 8. The seal is formed through the mutual extrusion of the outer side of the sealing ring (resembling a knife edge) and the inner wall of the sealing cylinder, resulting in plastic deformation. During the sealing process, a vertical downward force is applied to the upper face of the locking end cap, pressing the sealing ring into the sealing tube in excess, thereby forming a seal.

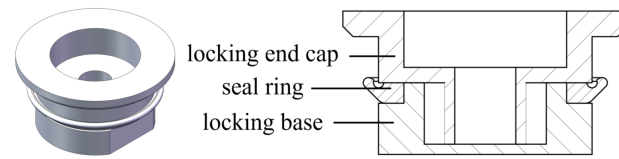


Figure 8. Lateral sliding seal.

#### 4. Finite Element Analysis of Sealing Performance

During extraterrestrial exploration, the demand for power consumption becomes increasingly stringent, directly impacting probe performance and efficiency. Consequently, in designing corresponding systems, minimizing power requirements for accomplishing tasks is paramount. In this design, the sealing actuation power serves as the primary criterion. The two aforementioned seal structures can be simplified into the schematic illustrated in Figure 9. Here, the left side of the central axis depicts the sliding seal, while the right side represents the non-sliding seal schematic. The overall seal configuration can be achieved by rotating along the central axis. Subsequent analysis will explore the impact of parameters labeled in Figure 9 on the seal actuation force. In addition to the parameters indicated in Figure 9, the effect of different cross-sectional shapes of the knife-edge configuration on the seal actuation force is considered for the non-sliding seal, as shown in Figure 10. Testing nearly two-hundred configurations by experimental means would consume significant time and incur high costs. Hence, utilizing the FEA method, with its low analysis cost and short turnaround time, is preferable, enhancing both design efficiency and cost-effectiveness.

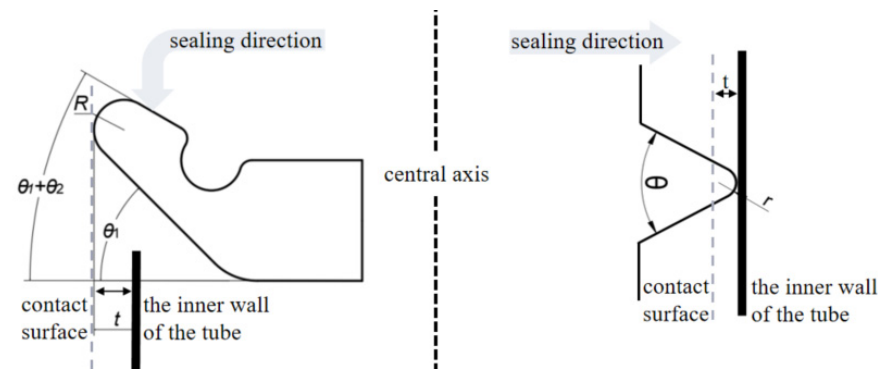


Figure 9. Simplified schematic of seal structure.

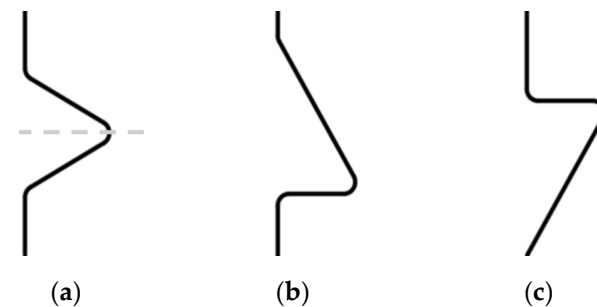


Figure 10. Different shapes of the knife edge: (a) symmetrical cross-sectional knife edge, (b) non-symmetrical cross-sectional knife edge I, and (c) non-symmetrical cross-sectional knife edge II.

##### 4.1. FEA Model

##### 4.1.1. Lateral Non-Sliding Seal

The static general module in ABAQUS is selected to simulate and analyze the sealing process. The specific parameters chosen for the knife edge are listed in Table 1. The overall

seal configuration can be achieved by rotating along the central axis. Consequently, in the FEA model, only the seal structure interface is constructed to reduce the computational scale. The constructed axisymmetric FEA model includes the seal cup, the ferrule, and a segment of the sample tube (length 16 mm). The ferrule spacer and circlip, which minimally affect the sealing actuation force, are excluded during model creation. A simplified model for simulating and analyzing the sealing process is depicted in Figure 11a.

**Table 1.** Specific parameters selected for the knife edge.

Names	Symbols	Values
Knife-edge angle	$\theta$	45/60/75
Knife-edge radius	$r$	0.025/0.05/0.1/0.2
Interference fit	$t$	0.2/0.3/0.4
Different shapes of the knife edge	/	Symmetrical/non-symmetrical I/non-symmetrical II

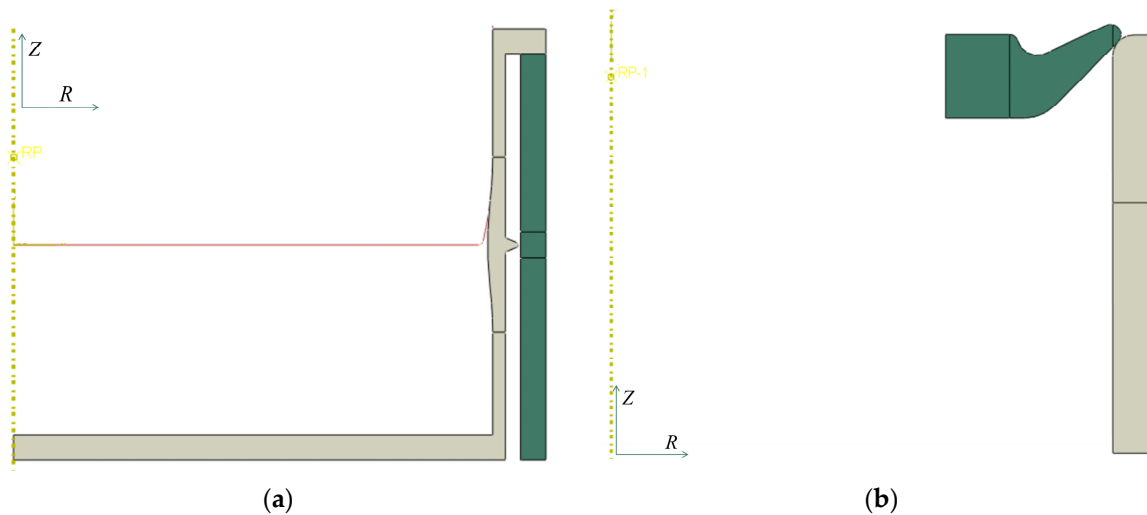


**Figure 11.** Axisymmetric FEA model: (a) lateral non-sliding seal FEA model, (b) lateral sliding seal FEA model.

#### 4.1.2. Lateral Sliding Seal

Due to the low loading speed of its seal actuating force, the static general module in ABAQUS is selected to simulate and analyze the sealing process. The specific parameters chosen for the sealing ring are listed in Table 2. The overall seal configuration can be achieved by rotating along the central axis. Consequently, in the FEA model, only the seal structure interface is constructed to reduce the computational scale. The locking end cap and locking base, which minimally affect the sealing actuation force, are excluded during model creation. The sample tube is partially retained, with its length preserved at twice the displacement distance of the sealing ring. A simplified model for simulating and analyzing the sealing process is depicted in Figure 11b.

**Table 2.** Specific parameters selected for the sealing ring.

Names	Symbols	Values
Angle of the bottom face	$\theta_1$	30/45/60
Angle of the top face	$\theta_2$	$\theta_1 - 10/\theta_1 - 20/\theta_1 - 30$
Interference fit	$t$	0.2/0.3/0.4/0.5
Tip radius	$r$	0.1/0.25/0.5/0.75

## 4.2. Material Properties' Parameters

### 4.2.1. Lateral Non-Sliding Seal

In the design of the lateral non-sliding seal structure, both the seal cup and sample tube are fabricated from TC4 titanium alloy, while the ferrule is designated as a rigid body. The material performance parameters are outlined in Table 3.

**Table 3.** Basic mechanical property parameters of materials.

Materials	Yield Strength/MPa	Modulus of Elasticity/MPa	Poisson's Ratio
Titanium alloy TC4	830	114,000	0.33
Stainless steel 304L	317	227,156	0.33
Stainless steel 316L	205	197,328	0.33
Aluminum alloy 6061Al	55	75,857	0.33
PEEK 450G	97	3500	0.4

### 4.2.2. Lateral Sliding Seal

In the design of the lateral sliding seal structure, the sealing ring is made of PEEK 450G and the sample tube is made of 6061 aluminum alloy. The material performance parameters are shown in Table 3.

## 4.3. Boundary Conditions, Connections, and Load

### 4.3.1. Lateral Non-Sliding Seal

In the simulation, the bottom of the sample tube is fixed to prevent displacement in all global directions ( $R = \theta = Z = 0$ ), while the ferrule moves downward by  $-4$  mm along the  $Z$  direction, as depicted in Figure 12a. The outer face of the ferrule is set to be in surface-to-surface contact with the inner wall of the seal cup, with a coefficient of friction set to 0.25 [29]. The outer face of the knife edge is set to be in surface-to-surface contact with the inner wall of the sample tube, with no friction. The sample tube spout is connected to the sealing cup at the contact position by a "tie" constraint.

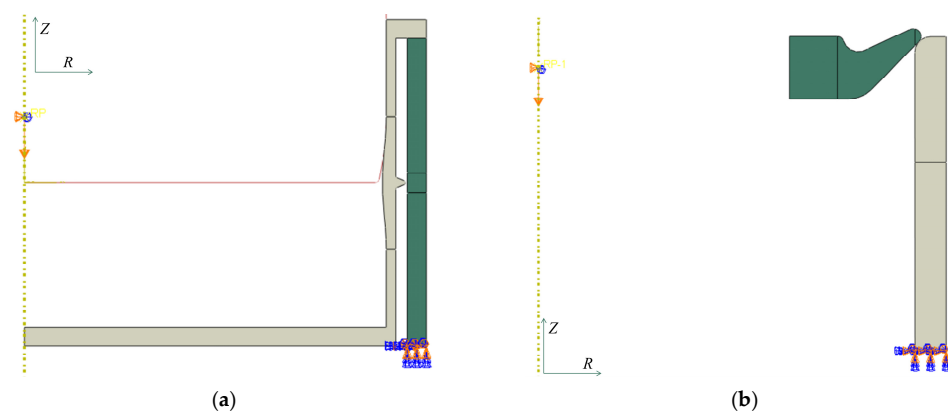


**Figure 12.** Boundary conditions, connections, and load. (a) lateral non-sliding seal, (b) lateral sliding seal.

### 4.3.2. Lateral Sliding Seal

In the simulation, the bottom of the sample tube is fixed to prevent displacement in all global directions ( $R = \theta = Z = 0$ ), while the sealing ring moves downward by  $-4$  mm along the  $Z$  direction, as depicted in Figure 12b. The outer lower face of the sealing ring is set to be in surface-to-surface contact with the inner wall of the sample tube, with a coefficient of friction set to 0.1 [33].

#### 4.4. Meshing

##### 4.4.1. Lateral Non-Sliding Seal

The sealing model utilizes CAX4R and CAX3 elements (the CAX4R element predominates). The basic element size of the seal cup is 0.2 mm, with grid refinement applied to its contact area with other components. Specifically, the tip of the knife edge is 0.005 mm, the side of the knife edge ranges from 0.005 to 0.02 mm, and the convex slope on the inner wall of the seal cup adjacent to the knife edge ranges from 0.05 to 0.1 mm. Within 1 mm above and below the contact area between the sample tube and the knife edge, the element size is 0.05 mm, while the rest of the sample tube uses 0.2 mm elements. Figure 13a depicts the mesh assembly. Subsequent to meshing, a quality check ensures consistent mesh normal vectors and Jacobian values exceeding 10, ensuring the accuracy and reliability of the calculations.

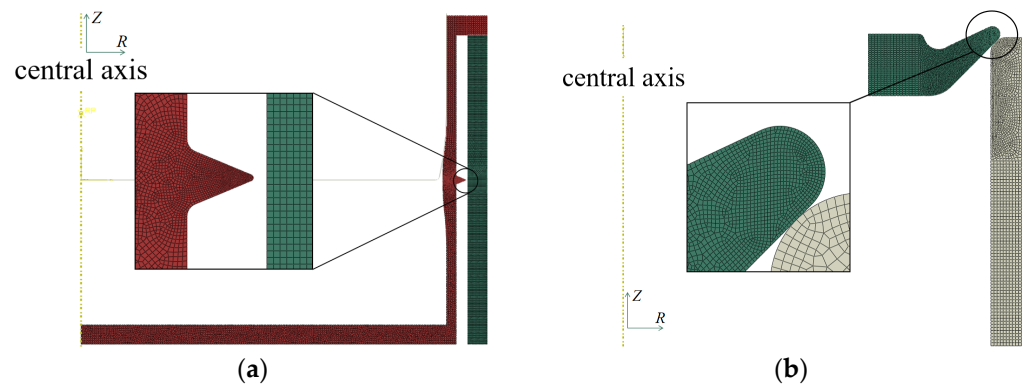


Figure 13. Meshing. (a) lateral non-sliding seal, (b) lateral sliding seal.

##### 4.4.2. Lateral Sliding Seal

The sealing model employs CAX4R and CAX3 elements (the CAX4R element predominates). The element sizes are as follows: 0.02 mm for the contact part of the sealing ring, 0.02 mm to 0.05 mm for other parts of the tip, and 0.1 mm for the section of the sealing ring between the locking end cap and the locking base. The inner wall of the sample tube in contact with the sealing ring is meshed with elements of size 0.05 mm, while the remainder of the tube uses elements of size 0.1 mm. Figure 13b illustrates the mesh assembly.

#### 4.5. FEA Results

##### 4.5.1. Lateral Non-Sliding Seal

The FEA results of the maximum actuation force for each knife edge are depicted in Figure 14. The FEA analysis is conducted under the same interference fit conditions. The three types of sealing structures, symmetrical and non-symmetrical (I/II) knife-edge shapes, are calculated and compared.

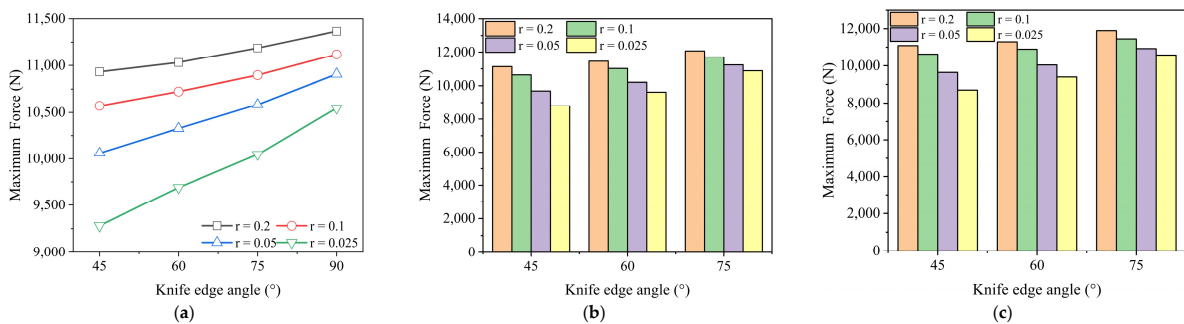


Figure 14. Maximum actuation force for each knife edge calculated by the FEA method: (a) symmetrical cross-sectional knife edge, (b) non-symmetrical cross-sectional knife edge I, and (c) non-symmetrical cross-sectional knife edge II.

As the symmetrical knife-edge shape, the maximum seal actuation force is 11.4 KN (knife-edge radius = 0.2 mm, and knife-edge angle =  $90^\circ$ ), while the minimum seal actuation force is 9.3 KN (knife-edge radius = 0.025 mm, and knife-edge angle =  $45^\circ$ ). For the non-symmetrical knife-edge shape, there are two configurations of cross-sectional knife-edge I (Figure 10b) and II (Figure 10c). For non-symmetrical knife-edge shape I, the maximum seal actuation force is 10.4 KN (knife-edge radius = 0.2 mm, and knife-edge angle =  $75^\circ$ ), and the minimum seal actuation force is 8.8 KN (knife-edge radius = 0.025 mm, and knife-edge angle =  $45^\circ$ ). For non-symmetrical tip shape II, the maximum seal actuation force is 11.9 KN (knife-edge radius = 0.2 mm, and knife-edge angle =  $75^\circ$ ), while the minimum seal actuation force is 8.7 KN (knife-edge radius = 0.025 mm, and knife-edge angle =  $45^\circ$ ).

The numerical results indicate that the maximum seal actuation force increases with both the knife-edge angle and the knife-edge radius for all knife-edge shapes.

However, in a longitudinal comparison of the maximum seal actuation force among different knife-edge shapes with the same knife-edge angle and radius, the symmetrical knife-edge structure exhibits the smallest maximum sealing actuation force (knife-edge radius = 0.1/0.2 mm), while the maximum sealing actuation force is observed for the other two knife-edge radii (knife-edge radius = 0.05/0.025 mm). This phenomenon arises due to the knife edge becoming thinner as the knife-edge radius decreases at low knife-edge angles (knife-edge angle =  $45^\circ/60^\circ$ ), resulting in greater torsional plastic deformation rather than interference plastic deformation during sealing. Consequently, the maximum seal actuation force for the asymmetric configuration is less than that for the symmetric configuration. Moreover, even at large knife-edge angles (knife-edge angle =  $75^\circ$ ), the maximum seal actuation force of the symmetric configuration remains smaller for the same knife-edge radius.

#### 4.5.2. Lateral Non-Sliding Seal in Other Materials

Through the above FEA results, the required sealing actuation force can be determined for the smallest knife edge. However, in this case, the sealing actuation force demand is as high as 8.7 KN. Therefore, alternative materials are demanded instead of titanium alloy. Considering the difficulty in manufacturing, the symmetrical configuration is chosen with a knife-edge angle of  $45^\circ$  and a knife-edge radius of 0.1 mm to explore the relationship between different interference fits, materials, and sealing force. The selected material parameters are shown in Table 3.

To investigate the effects of structure materials and interference fits on the sealing actuation force, FEAs are conducted and compared for materials including titanium alloy TC4, stainless-steel 304L, stainless-steel 316L, aluminum alloy 6061Al, and PEEK 450G, as illustrated in Figure 15. Interference fits of 0.2, 0.3, and 0.4 mm are applied at the initial assembly states. Based on the numerical results, the required seal actuation force for each structure material increases with a greater interference fit. TC4 demonstrates the highest seal actuation force for each initial interference fit (21.6 KN at 0.4 mm), while PEEK 450G exhibits the lowest seal actuation force. With an interference fit of 0.2 mm, only 1.34 KN of force is needed to achieve seal actuation for PEEK 450G.

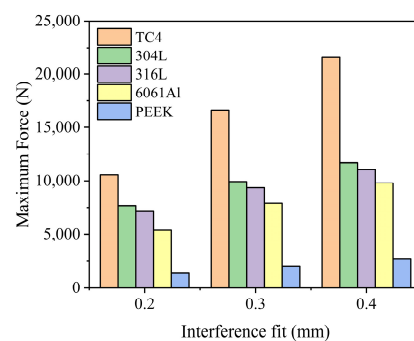


**Figure 15.** Maximum actuation force for different materials of the knife edge with a symmetrical configuration calculated by the FEA method.

Figure 16 illustrates the stress contours of the sealing retention position for each material, with a symmetrical tip configuration, a knife angle of 45°, a knife angle radius of 0.1 mm, and an interference fit of 0.2 mm.

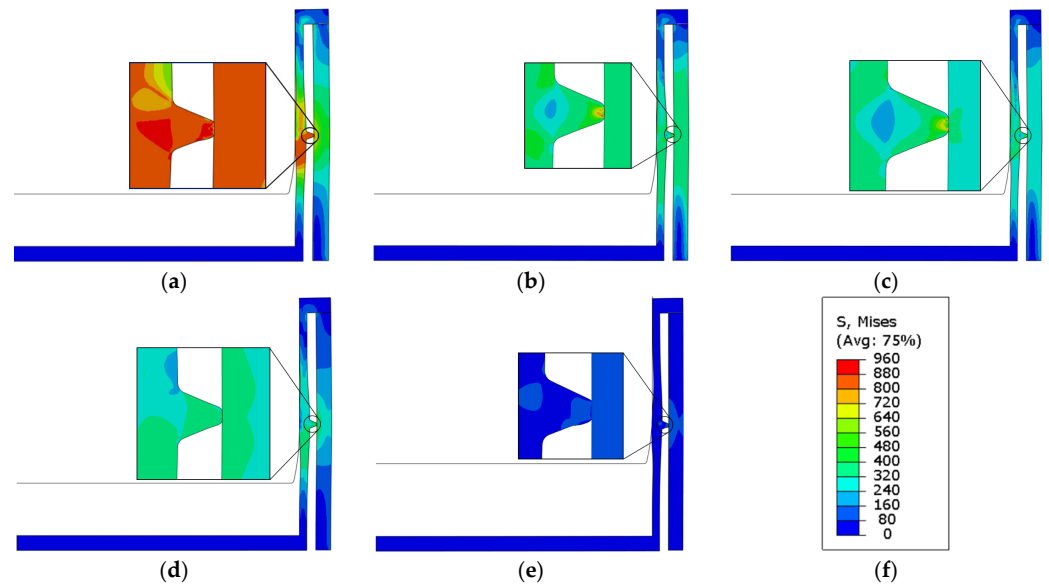


Figure 16. Stress contours: (a) TC4, (b) 304L, (c) 316L, (d) 6061Al, (e) PEEK, and (f) legend.

#### 4.5.3. Lateral Sliding Seal

According to the above FEA results, the seal actuation force of the PEEK material is much smaller than other materials; therefore, the seal ring is directly selected as the PEEK material for finite element analysis. The results of the maximum actuation force for each sealing ring are depicted in Figure 17. The FEA analysis is conducted under the same interference fit conditions. The maximum seal actuation force is calculated and compared for seal ring configurations with varying bottom face angles, differences in upper and lower end face angles, and tip radii.

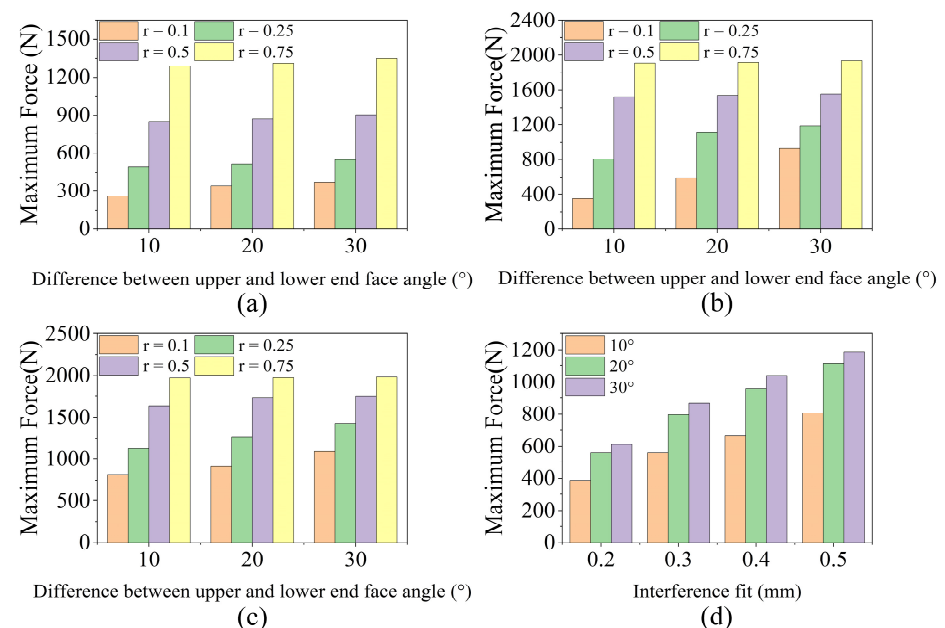


Figure 17. Maximum actuation force for each sealing ring calculated by the FEA method: (a)  $\theta_1 = 30^\circ$ , (b)  $\theta_1 = 45^\circ$ , (c)  $\theta_1 = 60^\circ$ , and (d) different interference fits of the seal structure.

For a sealing ring with a bottom face angle of  $30^\circ$ , the maximum seal actuating force is 1.35 kN (tip radius = 0.75 mm, and difference in upper and lower face angles =  $30^\circ$ ), and the minimum seal driving force is 0.25 kN (tip radius = 0.1 mm, and difference in upper and lower face angles =  $10^\circ$ ). For a sealing ring with a bottom face angle of  $45^\circ$ , the maximum seal actuating force is 1.93 kN (tip radius = 0.75 mm, and difference in upper and lower face angles =  $30^\circ$ ), and the minimum seal driving force is 0.35 kN (tip radius = 0.1 mm, and difference in upper and lower face angles =  $10^\circ$ ). For a sealing ring with a bottom face angle of  $60^\circ$ , the maximum seal actuating force is 1.98 kN (tip radius = 0.75 mm, and difference in upper and lower face angles =  $30^\circ$ ), and the minimum seal driving force is 0.82 kN (tip radius = 0.1 mm, and difference in upper and lower face angles =  $10^\circ$ ).

The numerical results indicate that the maximum seal actuation force increases with both the sealing ring tip radius and the difference between upper and lower end face angles for all sealing ring shapes.

Considering the machining difficulty and surface contact stresses, a sealing ring structure with a bottom face angle of  $45^\circ$  and a tip radius of 0.25 mm was used to explore the relationship between different angular differences ( $10^\circ$ ,  $20^\circ$ , and  $30^\circ$ ), different interference fits (0.2 mm, 0.3 mm, 0.4 mm, and 0.5 mm), and sealing forces. The FEA results are shown in Figure 17d.

From the above results, it is evident that the sealing actuation force of the sealing ring increases with the interference fit. Moreover, at the same interference fit, the sealing actuation force increases with the angular difference. The maximum sealing actuation force occurs when the angular difference is  $30^\circ$  at an interference fit of 0.5 mm, reaching 1.19 kN. Conversely, the minimum maximum sealing actuation force occurs when the angular difference is  $10^\circ$  at an interference fit of 0.2 mm, which is 0.39 kN.

Considering the aforementioned results, and accounting for factors such as machining difficulty, sealing actuation force, and surface contact stress, an interference fit of 0.3 mm, a bottom angle of  $45^\circ$ , an angular difference of  $20^\circ$ , and a tip radius of 0.25 mm have been selected. The maximum sealing force is calculated to be 0.8 kN. This configuration will serve as a reference for subsequent designs. Figure 18 shows a plot of the seal actuation force versus sealing ring downward displacement for selected sealing ring configurations in the FEA model, as well as a plot of the simulated state of the seal ring at a number of specific nodes labeled in the figure.

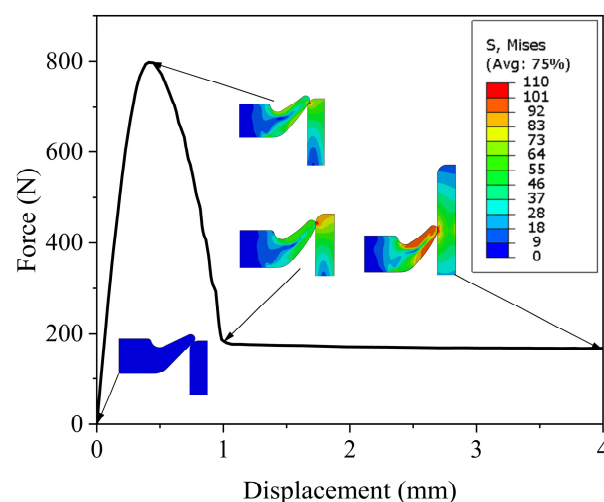


**Figure 18.** Seal actuation force versus sealing ring downward displacement.

## 5. Experiment

Through the FEA results in Section 4, the lateral sliding seal structure is identified as the optimal structure using the seal actuation force as the reference standard. In this

section, a seal and leakage rate test rig are designed to verify the actual actuation force and leakage rate of the selected seal structure.

### 5.1. Actuation Force Testing

The sealing operation of the sample tube system is executed by controlling the uniaxial testing machine indenter to move down the necessary stroke for sealing, while recording the force feedback during the downward pressure. The actual measured parameters of the sample seal assembly structure are summarized in Table 4. The specific experimental procedure is shown in Figure 19.

**Table 4.** Measured parameters.

Number	Inner Diameter of the Sample Tube	Seal Ring Outer Diameter
1	24.11 mm	24.40 mm
2	24.13 mm	24.40 mm
3	24.11 mm	24.38 mm

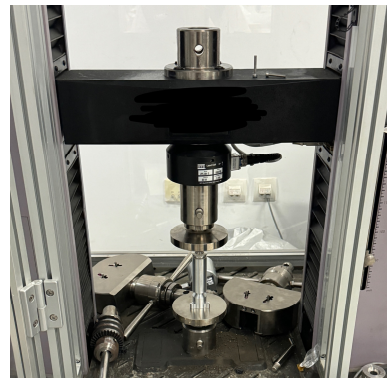


**Figure 19.** Actuation force testing of seals.

The force feedback of the sealing process of the sample tube, measured by the uniaxial testing machine, is compared with the corresponding theoretical analysis results via the FEA. As shown in Figure 20, the force–displacement curves of the testing data and FEA results represent the varying of the axial actuation force over the sealing process.

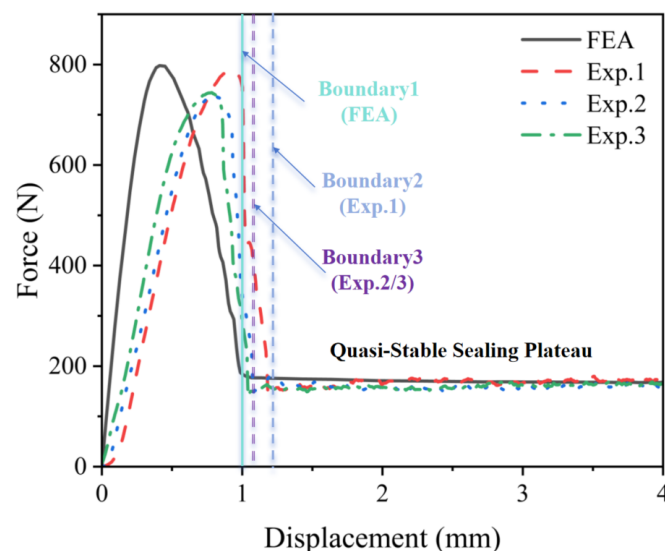


**Figure 20.** FEA results compared to test data.

The force increases with displacement at start, until reaching the peak value (maximum actuation force). In this period, the sealing ring undergoes radial compression, which transfers from an elastic deformation state to a plastic one. Then, the force descends with the displacement increasing due to deformation release and redistribution in both the sealing ring and contacted structure. Finally, the sealing structure achieves a steady state with the trivial fluctuation in force varying with displacement. The boundary line noted in the figure is marked as entering into a quasi-sealed state. The boundary lines colored as light green and blue (or purple) represent the FEA and experimental results, respectively.

It can be observed that the experimental results of each group are consistent with the theoretical analysis in the second half of the sealing process. Moreover, the displacement nodes reaching the quasi-stable sealing plateau generally correspond to the FEA results. However, slight discrepancies are observed in the experimental results during the first half of the sealing process, with the error in the maximum seal actuation force remaining within 5.8%. These differences may stem from minor inaccuracies in the processing of the sealing ring's outer diameter and the sealing tube's inner diameter. Since the load during the seal initiation phase is primarily influenced by the friction coefficient and the geometric interference of the components, the alignment of the experimental and simulated curves at the quasi-stable sealing plateau in the latter part of the sealing process underscores the suitability of the chosen friction coefficient. Deviations are attributed to machining errors in the sealing pairs or slight misalignment during assembly.

### 5.2. Leaking Rate Testing

In order to evaluate the sealing performance of the sealing structure, an external-pressure analog leakage detection device is established based on the actual sealing environment, as illustrated in Figure 21. The sample tube was secured within the chamber of the external-pressure analog container, and the chamber was pressurized with gas to create a differential pressure between the interior and exterior of the sealed container. This adjustable differential pressure environment allows for testing the sealing effectiveness of the container under varying pressure conditions.

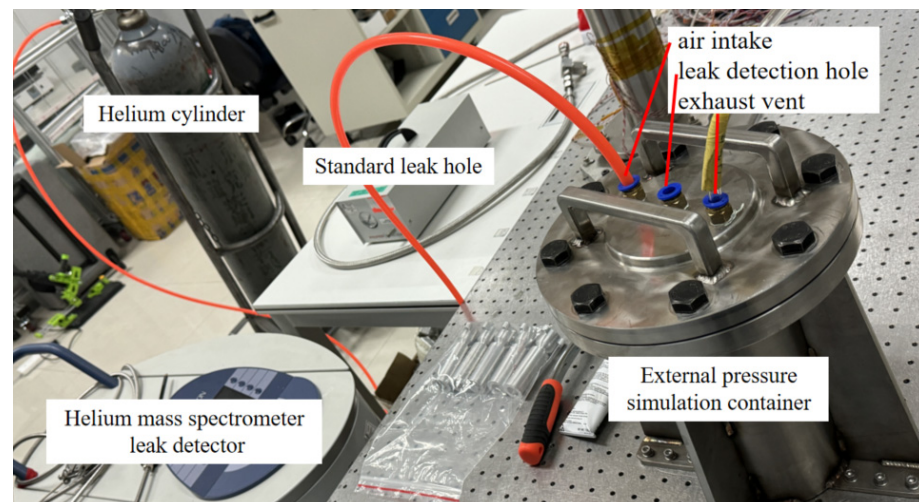
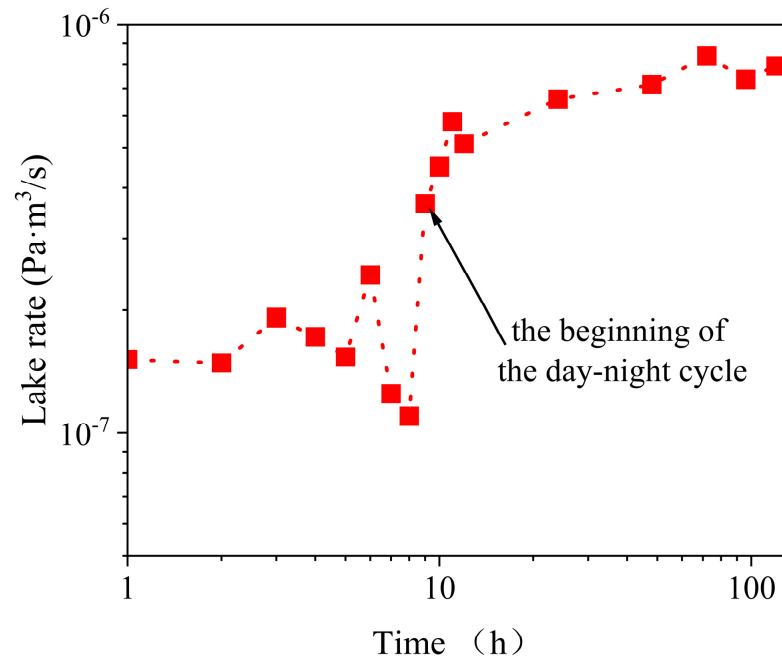


Figure 21. Leak rate testbed.

The results of the leaking rate test for the sample tube, subjected to an internal and external pressure difference of one atmosphere for 120 h, are depicted in Figure 22. Data were collected hourly for the first 12 h and then measured every 24 h thereafter.

The results indicate that the leakage rate of the sealing mechanism achieves a stable state after 10 h in laboratory-level experiments. The leaking rate can be maintained in the order of  $10^{-7} \sim 10^{-6}$  Pa·m<sup>3</sup>/s. The fluctuation in the curve within the first ten hours might be caused by room-temperature variation and measurement errors.



**Figure 22.** Long-time leakage rate test result.

### 5.3. Working Principle of Autonomous Sample-Collecting System

According to the system design scheme mentioned in Section 2, the prototype parts are processed to complete the assembly of the prototype.

The primary function of the motor in the sample tubes rotating mechanism and sealing end-cap rotating mechanism is to accurately position the sample tubes and sealing end caps. This function primarily entails position control, with no requirement for speed regulation. Both the sample tube rotating mechanism and sealing end-cap rotating mechanism are assembled with deep-groove ball bearings, resulting in a minimal actual load on the motor. Additionally, labor-saving gear transmission components with a 2:1 ratio are utilized. Therefore, torque indicators for the rotating motor are unnecessary. The MKS SERVO42D motor (Guangdong Maker Base, Guangdong, China) is selected here, and its electrical parameters are detailed in Table 5.

**Table 5.** Specifications of the motor.

Model	Values
Working voltage $U/V$	24
Maximum speed $\omega_{\max}/\text{rpm}$	3000
Holding torque $T/N\cdot\text{m}$	0.4
Step angle $\theta/^\circ$	1.8

This mechanical system solely serves as a sealing system. To execute the entire set of corresponding tasks, it must be integrated into the extraterrestrial mobile system and the drilling system. The ground mobile system utilizes the Unitree Go2 robot dog to carry the physical assembly of the entire machine system, as depicted in Figure 23. As shown in Figure 24, the workflow of the designed prototype is that the coring bit moves upward and the sample tube rotates to the position below the coring bit. Then, the pushing rod propels the sample from inside the core drill bit into the sample tube. Following this, the core drill bit ascends once more, and the sealing end cap rotates to directly above the sample tube. Finally, the coring bit descends, pressing the sealing end cap into the sealing tube to complete the sealing process.

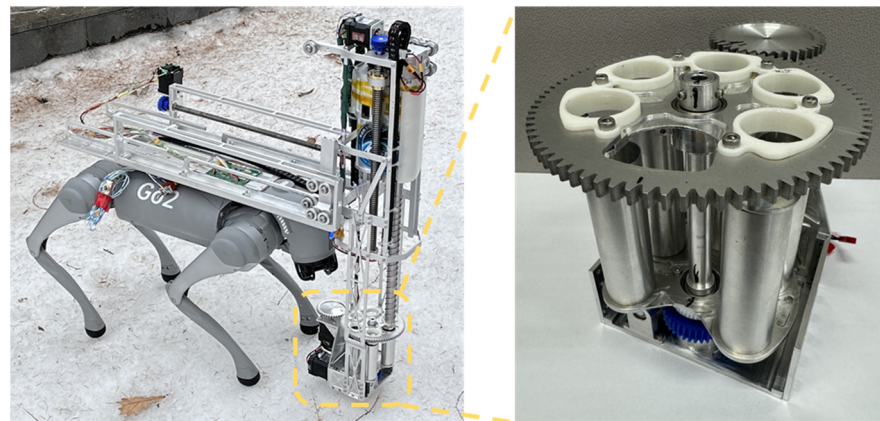


**Figure 23.** Sample sealing and coring systems integrated into the robotic platform.

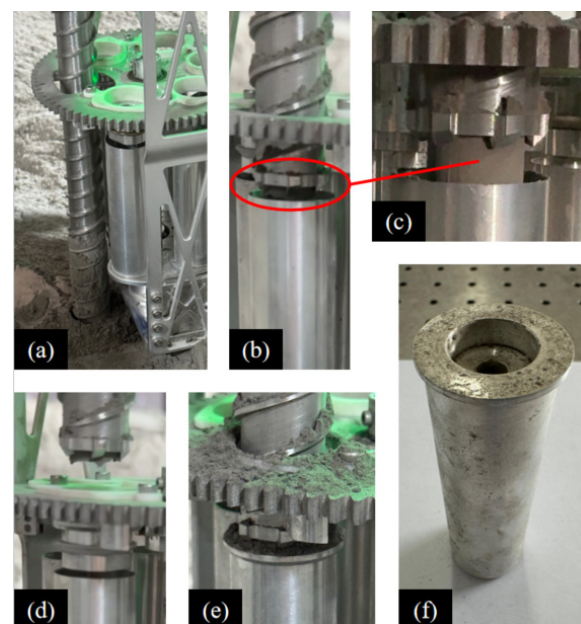


**Figure 24.** Workflow of automatic sealing mechanism: (a) the coring bit moves upward, (b) the sample tube rotates to the position below the coring bit, (c) the pushing rod propels the sample from inside the coring bit into the sample tube, (d) the core drill bit ascends once more, and the sealing end cap rotates to directly above the sample tube, (e) the coring bit descends, pressing the sealing end cap into the sealing tube, (f) sealed sample tube.

## 6. Future Study

To date, we have produced a set of automatic sealing mechanisms to verify the feasibility of the workflow. However, the experiments conducted in this paper are based on Earth's environment. In the actual process of extraterrestrial sampling, the working environment differs significantly from that on Earth, including variations in temperature, radiation, and vacuum conditions. Therefore, it is essential to simulate the corresponding extraterrestrial environment for further experimental verification.

Additionally, it is necessary to enhance the thermal design of the automatic sealing mechanism to improve the reliability of the entire system in low-temperature environments.

## 7. Conclusions

This paper outlines a sealing system design for extraterrestrial sampling. It includes multiple sample tubes for separate sealing operations, with feasibility confirmed through experiments. The study explores the impact of various geometric parameters on the actuation

force of lateral knife-edge seal structures employing two deformation mechanisms. Parametric numerical analysis reveals that the optimal configuration for a low actuation force includes a lateral sliding seal structure, PEEK material, a 0.25 mm tip radius, 0.3 mm interference, a 45° angle of the lower face, and a 20° difference between the upper and lower face angles. The sealing structure is tested for long-term leakage rate, and the leakage rate is kept in the order of  $10^{-7}$ – $10^{-6}$  Pa·m<sup>3</sup>/s for 120 h. The sealing mechanism is relatively compact, with measured overall dimensions of 152 mm × 180 mm × 123 mm, and a weight of 326 g. In conclusion, this work presents a novel design exploration aimed at enabling autonomous sampling sealing for extraterrestrial missions. Future research will focus on further examining the environmental feasibility of this design under extraterrestrial conditions.

**Author Contributions:** Conceptualization, H.Z. and Y.M.; methodology, Y.M., Z.Y. and R.M.; software, Y.M.; validation, Y.M., Z.N., X.L., T.G., T.D., Z.W. and R.H.; investigation, Y.M.; writing—original draft preparation, Y.M.; writing—review and editing, H.Z. and Z.S.; supervision, H.Z.; project administration, H.Z.; funding acquisition, H.Z. All authors have read and agreed to the published version of the manuscript.

**Funding:** The corresponding author H.F. Zhao acknowledges the support from the China Manned Space Engineering Program. The corresponding author Z.X. Shen acknowledges the support from the Hebei Provincial Natural Science Foundation, under Grant No. A2021203011.

**Data Availability Statement:** The datasets generated and supporting the finds of this article are available from the corresponding authors upon request.

**Conflicts of Interest:** The authors declare no conflicts of interest.

## References

1. Kemurdzhian, A.; Gromov, V.; Cherkasov, I.; Shvarev, V. Automatic stations for investigation of the lunar surface. In *Automatic Stations for Investigation of the Lunar Surface*; Mashinostroenie: Moscow, Russia, 1976; pp. 23–25.
2. Marov, M.Y.; Huntress, W. Soviet Robots in the Solar System. In *Mission Technologies and Discoveries*; Springer-Praxis: Chichester, UK, 2011; pp. 219–226.
3. Shi, X.; Deng, Z.; Quan, Q.; Tang, D.; Hou, X.; Jiang, S. Development of a drilling and coring test-bed for lunar subsurface exploration and preliminary experiments. *Chin. J. Mech. Eng.* **2014**, *27*, 673–682. [[CrossRef](#)]
4. Vinogradov, A. Preliminary data on lunar soil collected by the Luna 20 unmanned spacecraft. *Geochim. Cosmochim. Acta* **1973**, *37*, 721–729. [[CrossRef](#)]
5. Robinson, M.; Plescia, J.; Jolliff, B.; Lawrence, S. Soviet lunar sample return missions: Landing site identification and geologic context. *Planet. Space Sci.* **2012**, *69*, 76–88. [[CrossRef](#)]
6. Yada, T.; Fujimura, A.; Abe, M.; Nakamura, T.; Noguchi, T.; Okazaki, R.; Nagao, K.; Ishibashi, Y.; Shirai, K.; Zolensky, M.E. Hayabusa-returned sample curation in the Planetary Material Sample Curation Facility of JAXA. *Meteorit. Planet. Sci.* **2014**, *49*, 135–153. [[CrossRef](#)]
7. Dirri, F.; Longobardo, A.; Palomba, E.; Hutzler, A.; Ferrière, L. Basic design of sample container for transport of extraterrestrial samples. In Proceedings of the European Planetary Science Congress, Riga, Latvia, 17–22 September 2017; p. EPSC2017-2811.
8. Allton, J.; Bagby, J., Jr.; Stabekis, P. Lessons learned during Apollo lunar sample quarantine and sample curation. *Adv. Space Res.* **1998**, *22*, 373–382. [[CrossRef](#)]
9. Allton, J.H. *Catalog of Apollo Lunar Surface Geological Sampling Tools and Containers*; Lyndon, B., Ed.; Johnson Space Center: Houston, TX, USA, 1989; pp. 48–62.
10. Okazaki, R.; Sawada, H.; Yamanouchi, S.; Tachibana, S.; Miura, Y.N.; Sakamoto, K.; Takano, Y.; Abe, M.; Itoh, S.; Yamada, K. Hayabusa2 sample catcher and container: Metal-seal system for vacuum encapsulation of returned samples with volatiles and organic compounds recovered from C-type asteroid Ryugu. *Space Sci. Rev.* **2017**, *208*, 107–124. [[CrossRef](#)]
11. Sawada, H.; Okazaki, R.; Tachibana, S.; Sakamoto, K.; Takano, Y.; Okamoto, C.; Yano, H.; Miura, Y.; Abe, M.; Hasegawa, S. Hayabusa2 sampler: Collection of asteroidal surface material. *Space Sci. Rev.* **2017**, *208*, 81–106. [[CrossRef](#)]
12. Ji, M.; Sun, L.; Yang, M. Seal Design and Test Verification of Lunar Sample Container. *IOP Conf. Ser. Mater. Sci. Eng.* **2018**, *439*, 042025. [[CrossRef](#)]
13. Zhang, B.; Yu, M.; Yang, H. Leakage analysis and ground tests of the O-type rubber ring seal applied in lunar sample return devices. *Proc. Inst. Mech. Eng. Part G J. Aerosp. Eng.* **2015**, *229*, 479–491. [[CrossRef](#)]
14. Zhang, B.; Hong, H.; Yu, M.; Yang, H. Leakage analysis and ground tests of knife edge indium seal to lunar sample return devices. *Proc. Inst. Mech. Eng. Part G J. Aerosp. Eng.* **2019**, *233*, 2010–2022. [[CrossRef](#)]

15. Bar-Cohen, Y.; Badescu, M.; Bao, X.; Lee, H.J.; Sherrit, S.; Freeman, D.; Campos, S. Synchronous separation, seaming, sealing and sterilization (S4) using brazing for sample containerization and planetary protection. In Proceedings of the Sensors and Smart Structures Technologies for Civil, Mechanical, and Aerospace Systems 2017, Portland, OR, USA, 25–29 March 2017; pp. 47–53.
16. Gershman, R.; Bar-Cohen, Y.; Hendry, M.; Stricker, M.; Dobrynin, D.; Morrese, A. Break-the-chain technology for potential Mars sample return. In Proceedings of the 2018 IEEE Aerospace Conference, Big Sky, MT, USA, 3–10 March 2018; pp. 1–21.
17. Younse, P.; de Alwis, T.; Backes, P.; Trebi-Ollennu, A. Sample sealing approaches for Mars Sample Return caching. In Proceedings of the 2012 IEEE Aerospace Conference, Big Sky, MT, USA, 3–10 March 2012; pp. 1–11.
18. Younse, P.; Aveline, D.; Bao, X.; Berisford, D.; Bhandari, P.; Budney, C.; Chen, F.; Cooper, M.; Chung, S.; Lewis, D. Sample Tube Sealing for Future Proposed Mars Sample Return Missions. In Proceedings of the Lunar and Planetary Science Conference (LPSC 2013), The Woodlands, TX, USA, 18–22 March 2013.
19. Bao, X.; Badescu, M.; Sherrit, S.; Bar-Cohen, Y.; Campos, S. Heating and thermal control of brazing technique to break contamination path for potential Mars sample return. In Proceedings of the Sensors and Smart Structures Technologies for Civil, Mechanical, and Aerospace Systems 2017, Portland, OR, USA, 25–29 March 2017; pp. 173–180.
20. Backes, P.; Onstott, T.; Bar-Cohen, Y.; Badescu, M.; Pratt, L.; Helmick, D.; Sherrit, S.; Johnson, A.; Bao, X. Planetary sample sealing for caching. In Proceedings of the 2009 IEEE Aerospace Conference, Big Sky, MT, USA, 7–14 March 2009; pp. 1–10.
21. Wang, J.; Li, D.; Liu, K.; Wang, Z.; Qing, G.; Wang, Y.; Yan, C.; He, C.; Zhang, R. Numerical and experimental investigation of an automatic brazing vacuum seal system for Mars soil sample return. *Vacuum* **2024**, *219*, 112687. [[CrossRef](#)]
22. Bement, L.; Sanok, J. Explosive Joining for the Mars Sample Return Mission. In Proceedings of the 36th AIAA/ASME/SAE/ASEE Joint Propulsion Conference and Exhibit, Las Vegas, NV, USA, 24–28 July 1998; p. 3406.
23. Wang, J.; Li, X.; Yan, H.; Wang, X.; Wang, Y. Research on titanium-copper explosive welding interface with different welding parameters. *Int. J. Adv. Manuf. Technol.* **2022**, *122*, 3595–3606. [[CrossRef](#)]
24. Zhang, B.; Yu, M.; Yang, H.; Hong, H. Research on sealing structure and ground test of lunar sample return devices. In Proceedings of the ASME International Mechanical Engineering Congress and Exposition, San Diego, CA, USA, 15–21 November 2013; p. V001T001A029.
25. Zacny, K.; Craft, J.; Yachbes, I.; Mumm, E.; Ji, J.; Gorevan, S. Honeybee Robotics approach to technology development and infusion. In Proceedings of the 2010 IEEE Aerospace Conference, Big Sky, MT, USA, 6–13 March 2010; pp. 1–7.
26. Bao, X.; Younse, P.; Bhandari, P. FE simulation of SMA seal for Mars sample return. In Proceedings of the Sensors and Smart Structures Technologies for Civil, Mechanical, and Aerospace Systems 2013, San Diego, CA, USA, 10–14 March 2013; pp. 1228–1236.
27. Bao, X.; Younse, P. Finite element analysis of seal mechanism using SMA for Mars sample return. In Proceedings of the Sensors and Smart Structures Technologies for Civil, Mechanical, and Aerospace Systems 2014, San Diego, CA, USA, 9–13 March 2014; pp. 966–974.
28. Wang, J.; Li, D.; Zhang, R.; Wang, Y.; Qing, G.; Liu, K.; Xie, Y.; He, C. Experimental and analytical studies on behavior of shape memory alloy-based knife-edge seal system for extraterrestrial soil sample return mission. *Vacuum* **2024**, *222*, 113048. [[CrossRef](#)]
29. Redmond, L.; Kriechbaum, K.; Younse, P.; Kulczycki, E. Design of Robust Sealing Mechanism for Mars 2020 Sample Tubes. *J. Spacecr. Rocket.* **2020**, *57*, 964–974. [[CrossRef](#)]
30. Osterhout, J.T.; Farley, K.A.; Wadhwa, M.; Treffkorn, J.; Kulczycki, E. Helium Leak Rate Measurements of Flight-like Mars 2020 Sample Tubes. *Astrobiology* **2024**, *24*, 36–43. [[CrossRef](#)] [[PubMed](#)]
31. Moeller, R.C.; Jandura, L.; Rosette, K.; Robinson, M.; Samuels, J.; Silverman, M.; Brown, K.; Duffy, E.; Yazzie, A.; Jens, E. The Sampling and Caching Subsystem (SCS) for the scientific exploration of Jezero crater by the Mars 2020 Perseverance rover. *Space Sci. Rev.* **2021**, *217*, 5. [[CrossRef](#)]
32. Yang, J.; Li, X.; Tian, Z.; Wang, Z.; Han, R.; Yuan, Z.; Mu, R.; Zhao, H. Design of a Lunar Regolith Sampling System for Large-Scale Rover Traversals. In Proceedings of the 2023 IEEE International Conference on Real-time Computing and Robotics (RCAR), Datong, China, 17–20 July 2023; pp. 87–92.
33. Lind, J.; Lindholm, P.; Qin, J.; Rudolph, Å.K. Friction and wear studies of some PEEK materials. *Tribol. Finn. J. Tribol.* **2015**, *33*, 20–28.

**Disclaimer/Publisher’s Note:** The statements, opinions and data contained in all publications are solely those of the individual author(s) and contributor(s) and not of MDPI and/or the editor(s). MDPI and/or the editor(s) disclaim responsibility for any injury to people or property resulting from any ideas, methods, instructions or products referred to in the content.